M-sequence geomagnetic polarity time scale (MHTC12) that steadies global spreading rates and incorporates astrochronology constraints

Alberto Malinverno,[1] Jordan Hildebrandt,[2] Masako Tominaga,[3] and James E. T. Channell[4]

Received 27 February 2012; revised 16 May 2012; accepted 21 May 2012; published 30 June 2012.

[1] Geomagnetic polarity time scales (GPTSs) have been constructed by interpolating between dated marine magnetic anomalies assuming uniformly varying spreading rates. A strategy to obtain an optimal GPTS is to minimize spreading rate fluctuations in many ridge systems; however, this has been possible only for a few spreading centers. We describe here a Monte Carlo sampling method that overcomes this limitation and improves GPTS accuracy by incorporating information on polarity chron durations estimated from astrochronology. The sampling generates a large ensemble of GPTSs that simultaneously agree with radiometric age constraints, minimize the global variation in spreading rates, and fit polarity chron durations estimated by astrochronology. A key feature is the inclusion and propagation of data uncertainties, which weigh how each piece of information affects the resulting time scale. The average of the sampled ensemble gives a reference GPTS, and the variance of the ensemble measures the time scale uncertainty. We apply the method to construct MHTC12, an improved version of the M-sequence GPTS (Late Jurassic-Early Cretaceous, ~160–120 Ma). This GPTS minimizes the variation in spreading rates in a global data set of magnetic lineations from the Western Pacific, North Atlantic, and Indian Ocean NW of Australia, and it also accounts for the duration of five polarity chrons established from astrochronology (CM0r through CM3r). This GPTS can be updated by repeating the Monte Carlo sampling with additional data that may become available in the future.

Citation: Malinverno, A., J. Hildebrandt, M. Tominaga, and J. E. T. Channell (2012), M-sequence geomagnetic polarity time scale (MHTC12) that steadies global spreading rates and incorporates astrochronology constraints, *J. Geophys. Res.*, *117*, B06104, doi:10.1029/2012JB009260.

1. Introduction

[2] Over a wide range of Earth science disciplines, new insights require reliable reference time scales. Because polarity reversals of the geomagnetic field are globally synchronous, the construction of a Late Cretaceous-Cenozoic geomagnetic polarity time scale (GPTS) has been a crucial step in geologic time scale development. The GPTS has now become the scale to which other facets of geologic time are correlated [*Heirtzler et al.*, 1968; *Cande and Kent*, 1992; *Opdyke and Channell*, 1996; *Ogg and Smith*, 2004; *Gee and Kent*, 2007]. Since the seminal paper of *Shackleton et al.* [1990], rapid progress has been made in improving Cenozoic time scales by calibrating the GPTS with astrochronologies from magnetostratigraphically controlled sediment sections [e.g., *Hilgen*, 1991; *Billups et al.*, 2004; *Lourens et al.*, 2004; *Pälike et al.*, 2006].

[3] Oceanic crust also records M-sequence (Late Jurassic-Early Cretaceous) magnetic anomalies, and GPTSs for this interval have been constructed by interpolating a few radiometric dates and assuming constant or uniformly varying spreading rates in a subset of all the available magnetic anomaly profiles [e.g., *Larson and Hilde*, 1975; *Channell et al.*, 1995; *Tominaga and Sager*, 2010]. In the Mesozoic, uncertainties in orbital solutions preclude direct temporal correlations, and astrochronology can only constrain durations (e.g., of polarity chrons) but does not provide absolute age information [*Hinnov*, 2004]. The marine magnetic anomaly record provides the template for polarity reversal and is therefore indispensable for constructing a M-sequence GPTS. Because of the lack of reliable radiometric ages for the M-sequence GPTS, limitations of available astrochronologies, and reliance on the assumption of constant spreading rates, uncertainties in the Late Jurassic-Early Cretaceous time scales are the highest in the Phanerozoic and reach ±4 Myr according to *Hinnov and Ogg* [2007].

[1]Lamont-Doherty Earth Observatory, Earth Institute at Columbia University, Palisades, New York, USA.
[2]Department of Geology, Wittenberg University, Springfield, Ohio, USA.
[3]Woods Hole Oceanographic Institution, Woods Hole, Massachusetts, USA.
[4]Department of Geological Sciences, University of Florida, Gainesville, Florida, USA.

Corresponding author: A. Malinverno, Lamont-Doherty Earth Observatory, Earth Institute at Columbia University, 61 Route 9W, Palisades, NY 10964, USA. (alberto@ldeo.columbia.edu)

0148-0227/12/2012JB009260

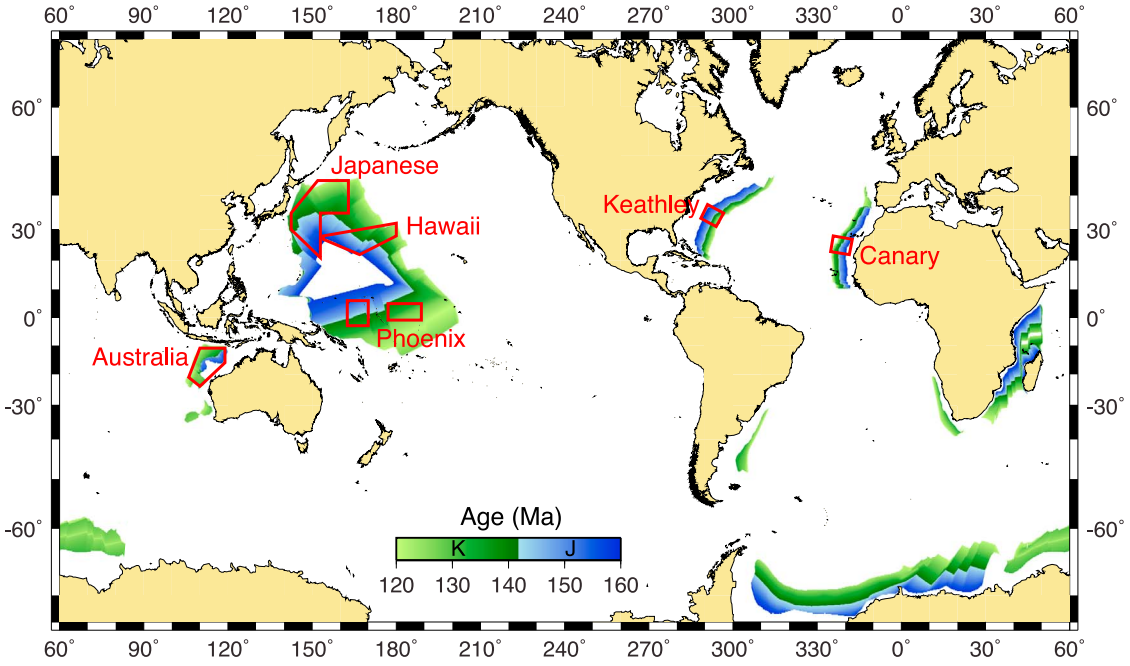

Figure 1. Red boxes indicate ocean floor areas with the M-sequence magnetic lineations used in this study. The shaded background shows 120–160 Ma oceanic crust where M-sequence magnetic anomalies have been observed from the age grid of *Müller et al.* [2008], with Cretaceous (K) ages in green and Jurassic (J) in blue.

[4] Here, we provide an updated M-sequence GPTS, named MHTC12, that addresses some of the shortcomings of previous attempts. Following the "least favoritism" principle advocated by *Huestis and Acton* [1997], the GPTS obtained here minimizes the global variability of spreading rates in all the available marine magnetic anomaly sequences, thereby replacing the necessity for a constant spreading rate assumption. Moreover, MHTC12 includes information on polarity chron durations estimated from astrochronology. This integration is accomplished by propagating uncertainties from the input data, which weigh the extent to which each piece of information constrains the final GPTS. We argue that such an integration of diverse data sources is an advance from the usual "winner-take-all" strategy where the GPTS is based on the set of data deemed most accurate (e.g., a selected set of magnetic lineations).

2. Background

2.1. Notation

[5] Following general nomenclature [*Opdyke and Channell*, 1996; *Gee and Kent*, 2007], M-sequence magnetic anomalies are named M0r, M1n, etc., and the corresponding polarity chrons are CM0r, CM1n, etc. Magnetic polarity is explicitly noted by appending "n" for normal and "r" for reversed. We denote years of age as "a" and years of duration as "yr," with the usual prefixes (e.g., 1 Ma = 1 million years ago).

2.2. Previous M-Sequence GPTSs

[6] The M-sequence magnetic anomalies have been mapped in the oldest parts (about 120–160 Ma) of the world's oceans, and the best continuous lineation sets can be found in the Western Pacific, Northern Atlantic, and Indian Ocean NW of Australia (Figure 1); available studies are summarized by *Tominaga and Sager* [2010]. Several M-sequence GPTSs have been constructed by assuming constant spreading rates between radiometric dates in the Hawaiian magnetic lineations [*Larson and Pitman*, 1972; *Larson and Hilde*, 1975; *Channell et al.*, 1995]. The most recent of these time scales [*Channell et al.*, 1995], hereafter referred to as CENT94, is based on a single magnetic anomaly profile in the Hawaiian lineations and three dates for CM0, CM16, and CM25.

[7] In the most recent Geological Time Scale compilation [*Gradstein et al.*, 2004], *Ogg and Smith* [2004] constructed a M-sequence GPTS with a composite magnetic anomaly record based on the Hawaiian lineations in the M0-M25n interval, the Japanese lineations in the M25r-M27n interval [*Handschumacher et al.*, 1988], and a deep-tow survey of the Japanese lineations in the M27r-M41 interval [*Sager et al.*, 1998]. In this GPTS, hereafter named GTS2004, *Ogg and Smith* [2004] used a "minimalist" spreading rate model (four intervals of constant spreading rate separated by small jumps or linear changes), three radiometric age constraints (for CM0, CM26, and CM41), and a few polarity chron durations from astrochronology (see below). Although GTS2004 goes back to CM41, acceptance of the pre-CM29 reversal record has been debated because these anomalies have low amplitudes and the record is only from one spreading system, the Japanese lineation set [*Sager et al.*, 1998; *Tominaga et al.*, 2008]. To date, CM29 is the oldest chron where higher amplitude magnetic anomaly lineations are available from multiple locations, and we focus on the CM0-CM29 interval in this paper.

[8] Most recently, *Tominaga and Sager* [2010] constructed a GPTS for the CM0-CM29 interval based on an updated set of 52 magnetic anomaly profiles from the Pacific

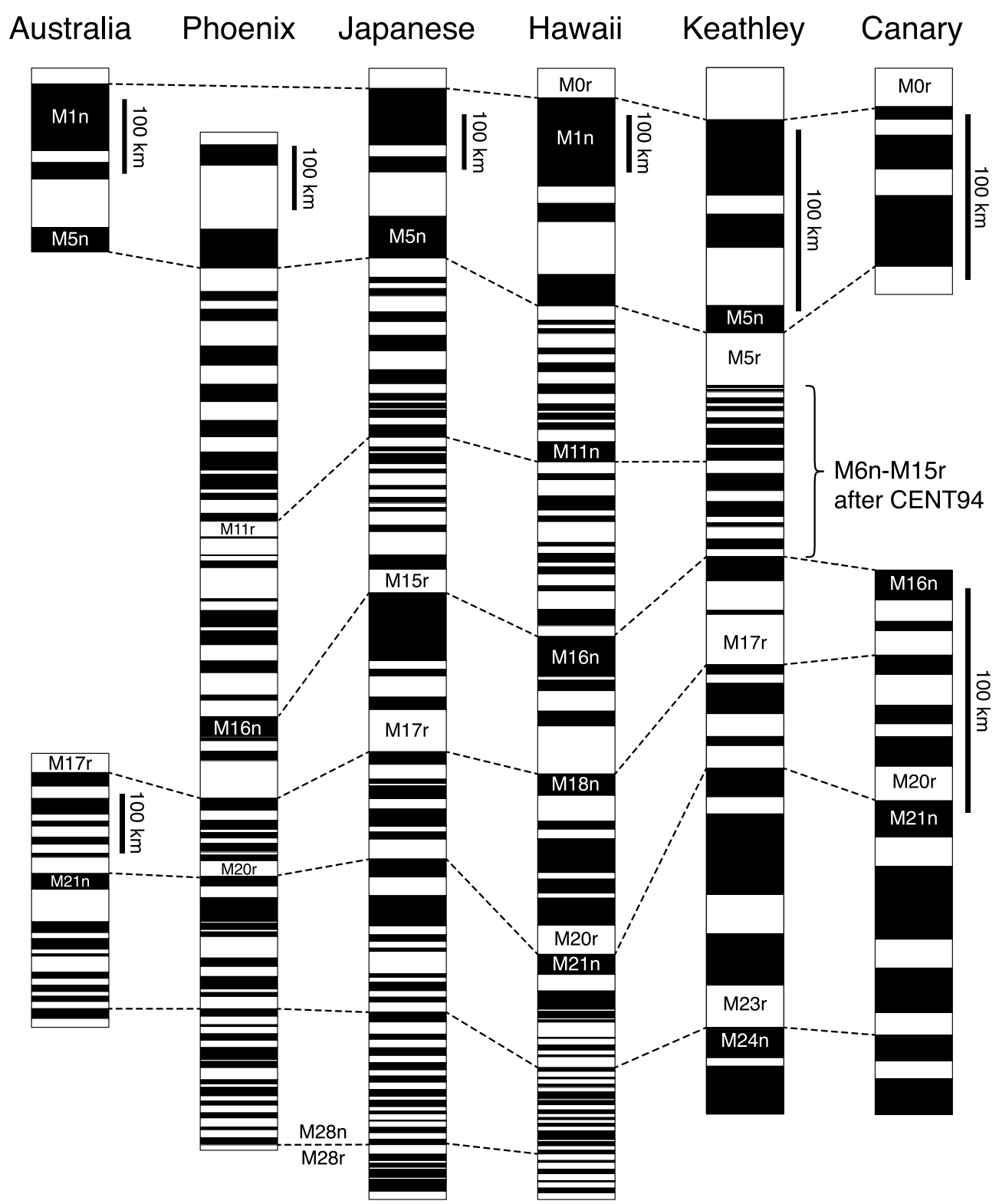

Figure 2. Block model distances used in this study, after TS10 except for the interval M6n-M15r in the Keathley block model, which was not included in the TS10 compilation. Data in this interval were inserted using the distances published in CENT94. Note the different distance scales.

(Figure 2). Their GPTS, hereafter named TS10, is not built assuming a constant spreading rate on a single set of lineations. Instead, TS10 is based on a composite profile obtained by averaging rescaled distances measured on the Hawaiian, Japanese and Phoenix lineations, and is constrained by two age calibration points (CM0 and CM26). This is equivalent to assigning a constant spreading rate to the composite profile and assuming a constant ratio of spreading rates between

the three lineation sets. The up-to-date magnetic block model data published by TS10 will be the basis for the GPTS presented here.

[9] The GPTSs described above relied on the assumption of constant (or smoothly varying) spreading rates in a limited set of magnetic lineations. It was also recognized, however, that a valid GPTS should result in small spreading rate fluctuations on other ridges [*Cande and Kent*, 1992; *Channell et al.*, 1995]. *Huestis and Acton* [1997] pointed out that there is no a priori reason to expect that spreading rates vary smoothly at one particular location while they fluctuate more erratically at all other ridges. They argued for a global approach where a GPTS is constructed by minimizing the spreading rate variation in all the magnetic anomaly lineations examined and ran a test inversion on a demonstration data set. We adopt the same philosophy and add uncertainty quantification in the GPTS construction process.

2.3. Astrochronology in the Mesozoic

[10] Over the last few decades, time series analyses of sediment properties have conclusively shown periodicities linked to Milankovitch orbital cycles [e.g., *Hays et al.*, 1976; *Martinson et al.*, 1987]. This discovery sparked considerable interest in using orbital cycles to measure time in the geological record, and astronomical cycle stratigraphy started its development [*Fischer et al.*, 1990; *Shackleton et al.*, 1990; *Hilgen*, 1991; *Schwarzacher*, 1993].

[11] In principle, an astronomically based time scale can be constructed by correlating records of sediment properties controlled by climate (e.g., carbonate content) with orbital solutions (for eccentricity, obliquity, and precession) or with inferred insolation for a particular season and location. The most recent version of the Neogene geological time scale [*Lourens et al.*, 2004] represents a compilation of numerous such individual astrochronological studies.

[12] Neogene astrochronology has significant implications for global variations in oceanic spreading rates. *Wilson* [1993] and *Krijgsman et al.* [1999] found that the spreading rates implied by astronomical dating in the last 10 Ma were less variable than rates computed from the *Cande and Kent* [1992] GPTS; astronomical age control tends to steady spreading rates [see also *Gordon*, 1993; *Baksi*, 1994; *Langereis et al.*, 1994; *Krijgsman et al.*, 1999]. This observation supports the notion that minimizing global spreading rate fluctuations is a useful strategy to construct a GPTS [*Huestis and Acton*, 1997].

[13] Astronomical dating in the geological past beyond a few tens of Ma is more challenging than in the Cenozoic. The solar system is chaotic, and because of sensitivity to initial conditions the phases of orbital cycle solutions are accurate only to about 50 Ma [*Laskar*, 1999; *Laskar et al.*, 2004, 2011]. Astrochronology in the Mesozoic cannot, therefore, be based on direct temporal correlation, but instead relies on detecting periodicities in sedimentary records that correspond to supposed periods of orbital cycles. The resulting "floating" time scales constrain the duration of intervals but need independent information to obtain absolute ages [*Hinnov*, 2004]. An additional difficulty is that tidal dissipation progressively decreases the rotation rate of the Earth and increases the Earth-Moon distance, so that the obliquity and precession periods were shorter in the geologic past; on the other hand, the long eccentricity cycle (405 kyr) is expected to have remained rather constant throughout the Phanerozoic [*Berger et al.*, 1992; *Laskar et al.*, 2004, 2011].

[14] The duration of Mesozoic intervals have been estimated by counting bedding couplets and bundles interpreted to correspond to precession and eccentricity cycles [*Fischer and Schwarzacher*, 1984; *Herbert and Fischer*, 1986; *Herbert*, 1992; *Herbert et al.*, 1995; *Fiet and Gorin*, 2000] or by some form of spectral analysis [*Park and Herbert*, 1987; *Hinnov and Park*, 1998; *Meyers and Sageman*, 2007; *Meyers*, 2008; *Malinverno et al.*, 2010]. The durations of CM0 through CM2 estimated by *Herbert* [1992] were used to constrain GTS2004. In this study, we directly incorporate, into the GPTS construction process, the durations of CM0 through CM3 and their uncertainties estimated by astrochronology [*Fiet and Gorin*, 2000; *Malinverno et al.*, 2010].

3. Data

3.1. Magnetic Anomaly Block Model Distances

[15] The first step in GPTS construction is to generate block models consisting of alternating magnetic polarity intervals. The positions of polarity changes in these block models are adjusted to match measured magnetic anomaly profiles projected on a line perpendicular to the local strike of magnetic lineations and deskewed so that the anomalies are symmetrical. Two recent GPTS studies list M-sequence block model distances derived in this fashion, CENT94 [*Channell et al.*, 1995] and TS10 [*Tominaga and Sager*, 2010]. CENT94 constructed block models for the Western Pacific Hawaii (based on 1 profile), Japanese (6), and Phoenix lineations (4), supplemented by a North Atlantic Keathley block model computed from the spreading rates of *Klitgord and Schouten* [1986]. TS10 examined a larger set of magnetic anomaly profiles and built block models for the Western Pacific Hawaii (based on 11 profiles), Japanese (28), and Phoenix lineations (13), the Indian Ocean NW of Australia (7), and the North Atlantic Keathley (4) and Canary (7) lineations (Figure 1). The Western Pacific data in TS10 included 9 out of the 11 profiles used by CENT94. The block models of TS10 were built by averaging polarity boundaries determined for several profiles, thus reducing the noise due to irregularities in the crustal recording process, and are the most comprehensive up-to-date compilation. We use for our GPTS the TS10 block model distances, adding the distances given by CENT94 for the interval M6n-M15r in the Keathley block model (Figure 2). Our magnetic anomaly nomenclature follows TS10, except that M25Ar, M25n5, and M25r5 in TS10 have been changed to M25Ar.1r, M25Ar.1n, and M25Ar.2r, respectively, to follow general nomenclature rules [e.g., *Gee and Kent*, 2007].

3.2. Radiometric Dates

[16] Radiometric dates relevant to the GPTS in the CM0-CM29 time interval are listed in Table 1. Most of these dates do not have a direct or precise tie to the reversal sequence, and previous M-sequence GPTSs have been constructed on the basis of two (TS10) or three dates (CENT94, GTS2004). Our GPTS is constrained by two radiometric dates, and the GPTS ages we obtain will be later compared to all dates in Table 1.

[17] The first date used here is 121.2 $\pm$ 0.5 Ma for the middle of CM0r. This date is from the results of *He et al.*

Table 1. Radiometric Dates in the M-sequence Interval[a]

Radiometric Date (Ma)	Stratigraphic Age	Polarity Chron	Reference	Notes
121.2 ± 0.25	Aptian	Within CM0r	*He et al.* [2008]	Ar/Ar age for the TCR sanidine age of *Renne et al.* [1998]
124.6 ± 0.9	Barremian	Near end of CM1r[b]	*Pringle and Duncan* [1995]	Ar/Ar age corrected in GTS2004 to the TCR sanidine age of *Renne et al.* [1998]
136 ± 3	Late Valanginian	CM11r-CM12r	*Wan et al.* [2011]	SHRIMP U-Pb age. Correlation to magnetic stratigraphy after GTS2004
137 + 0.8/–0.3	Early part of late Berriasian	CM16n-CM16r	*Bralower et al.* [1990]	U-Pb zircon age
144.6 ± 0.4	Earliest Berriasian or younger	After onset of CM19n.2n	*Mahoney et al.* [2005]	Ar/Ar age for the FCT-3 biotite age of *Renne et al.* [1998]. Correlation to magnetic stratigraphy after GTS2004
155.3 ± 3.4	Oxfordian	End of CM26n	*Ludden* [1992]	K/Ar age. Polarity chron assignment after *Sager et al.* [1992]

[a]Uncertainties are one standard deviation.
[b]GTS2004 assigns this date to CM0r.

[2008] with an increased uncertainty to account for the unknown position of the dated material within CM0r, which lasts about 0.5 Myr. All uncertainties reported here are one standard deviation; radiometric age uncertainties are based on analytical error and do not therefore include uncertainties related to causes such as standard age uncertainty or sample alteration. *He et al.* [2008] dated reversely magnetized lavas in northeast China and argue that the ages of these volcanics correspond to CM0r. Their conclusion is consistent with the original interpretation of *Pringle and Duncan* [1995], who assigned to the end of CM1r a 124.6 Ma date measured on reversely magnetized basalt sampled at MIT Guyot (Table 1). An age of 121 Ma for the onset of CM0r was used in the CENT94 GPTS.

[18] The age of CM0r, however, is debated. The critical question is which reversed polarity chron is being dated by the work of *Pringle and Duncan* [1995]: CM0r or CM1r? *Ogg et al.* [2004] assigned the 124.6 Ma age of *Pringle and Duncan* [1995] to CM0r and concluded that the onset of CM0r (the Barremian-Aptian boundary) should be at 125 Ma. This age assignment is supported by a recent astrochronology from the Piobbico Core (Central Italy) that estimates an Aptian duration of 13.42 Myr and an age of 125.45 Ma for the Barremian-Aptian boundary [*Huang et al.*, 2010]. On the other hand, cyclostratigraphy of the same Piobbico Core and neighboring outcrops by *Herbert et al.* [1995] gave a duration of 10.1 Myr for the interval between the end of the Aptian and the end of CM0r, implying a Barremian-Aptian boundary at ∼122 Ma.

[19] The alternative age assignments for CM0r are discussed at length in the papers cited above. Our preference is for the 121 Ma date used in the CENT94 GPTS because it is difficult to reconcile a 125 Ma age for CM0r, which is the last reversed-polarity chron preceding the Cretaceous Long Normal superchron, with the radiometric date of 121.2 Ma measured in reversed-polarity volcanics by *He et al.* [2008]. The MHTC12 GPTS obtained here consequently assumes a date of 121.2 ± 0.5 Ma for the middle of CM0r. We recognize, however, that the age of CM0r is not settled, and we include in the auxiliary material an alternative GPTS, MHTC12–125, constructed in the same way as MHTC12 except for an age of 125 ± 0.5 Ma assigned to the onset of CM0r.[1]

[20] The second date used here is 155.3 ± 3.4 Ma assigned to the end of CM26n. This age was obtained by *Ludden* [1992] on a celadonite vein recovered from Ocean Drilling Program (ODP) Site 765 in the Argo Abyssal Plain. This age was assigned to the middle of CM26n by GTS2004, but the end of CM26n better matches the location of Site 765 in the polarity block model of *Sager et al.* [1992]. This is a minor difference given the large uncertainty of this date.

3.3. Chron Durations From Astrochronology

[21] The polarity chron durations from astrochronology used in this study are listed in Table 2. These chron durations, estimated by *Malinverno et al.* [2010] and by *Fiet and Gorin* [2000] on Cretaceous pelagic sequences in northern and central Italy, have been chosen because they are closely tied to a magnetic stratigraphy and include a quantified uncertainty. The durations of CM0r, CM1n, CM1r, and CM3n in Table 2 are the same (within uncertainties) as those estimated for CM0r by *Huang et al.* [2010] and for the other chrons by *Herbert* [1992].

4. Monte Carlo GPTS Construction

[22] The problem of GPTS construction can be stated as an inverse problem: find ages for polarity chron boundaries in a model parameter vector **m** that simultaneously agree with radiometric dates (vector **d**), minimize the variability of spreading rates evaluated from block model distances (vector **b**), and fit polarity chron durations from astrochronology (vector **c**). We apply a Bayesian formulation of the inverse problem [e.g., *Tarantola and Valette*, 1982; *Jackson and Matsu'ura*, 1985; *Duijndam*, 1988; *Malinverno*, 2002], where the solution is a posterior distribution of GPTS vectors that can be written as

$$p(\mathbf{m} \mid \mathbf{d}, \mathbf{b}, \mathbf{c}) = \text{const.} \times p(\mathbf{m}) p(\mathbf{d} \mid \mathbf{m})\, p(\mathbf{b} \mid \mathbf{m})\, p(\mathbf{c} \mid \mathbf{m}), \quad (1)$$

where $p(\mathbf{m})$ is a prior distribution and $p(\mathbf{d} \mid \mathbf{m})$, $p(\mathbf{b} \mid \mathbf{m})$, and $p(\mathbf{c} \mid \mathbf{m})$ are likelihood functions (the normalizing constant

Table 2. Chron Durations From Astrochronology Studies[a]

Polarity Chron	Estimated Duration (Myr)	Reference
CM0r	0.49 ± 0.05	*Malinverno et al.* [2010]
CM1n	2.28 ± 0.24	*Fiet and Gorin* [2000]
CM1r	0.43 ± 0.21	*Fiet and Gorin* [2000]
CM3n	0.7 ± 0.19	*Fiet and Gorin* [2000]
CM3r	1.75 ± 0.24	*Fiet and Gorin* [2000]

[a]Uncertainties are one standard deviation.

[1]Auxiliary materials are available in the HTML. doi:10.1029/2012JB009260.

can be ignored). The prior distribution is based on the expected statistical characteristics of the GPTS, and the likelihood functions measure how closely a given GPTS in the vector **m** agrees with the data in the vectors **d**, **b**, and **c**.

[23] A way to solve the inverse problem is to find an optimal GPTS as the value of **m** that maximizes the value of the posterior distribution in equation (1), for example using a nonlinear optimization method as done by *Huestis and Acton* [1997]. Optimization, however, does not quantify the uncertainty that is inherent to the GPTS, e.g., because of spreading rate fluctuations or imprecise dating constraints [*Agrinier et al.*, 1999]. Instead of striving to find a best value for the GPTS, we apply a Monte Carlo sampling method to obtain a large ensemble of possible GPTSs that agree with the data. The mean value of this ensemble will give the reference GPTS, and its variability will measure the uncertainty associated with the GPTS (e.g., quantified by the standard deviation of the sampled GPTS values). A similar strategy to obtain a GPTS using a genetic algorithm has been proposed by *Acton and Huestis* [1994].

[24] The sampling can be carried out efficiently by Markov chain Monte Carlo (MCMC) methods [*Gilks et al.*, 1996], which have been used extensively in geophysical inverse problems [e.g., *Mosegaard and Tarantola*, 1995; *Sen and Stoffa*, 1995; *Malinverno*, 2002; *Sambridge and Mosegaard*, 2002; *Sambridge et al.*, 2006]. In these methods, the vector **m** is iteratively modified to perform a random walk in the space of possible model parameters and each step in the random walk only depends on the previous value of **m** (the Markov property). We follow the practical strategy outlined by *Mosegaard and Tarantola* [1995], which can be broken in two parts. First, a random walk process generates a candidate GPTS that agrees with prior information on the distribution of polarity chron durations and with radiometric dates. The candidate GPTS is then accepted or rejected following the Metropolis algorithm [*Metropolis et al.*, 1953; *Chib and Greenberg*, 1995] depending on the extent it minimizes the total variability of spreading rates and how well it fits polarity chron durations from astrochronology. When repeated many times, this simple recipe samples an ensemble of GPTSs that will be asymptotically distributed as in the posterior distribution of equation (1) [*Mosegaard and Tarantola*, 1995]. Details on the implementation of the MCMC algorithm are in Appendix A, and in the rest of this section we illustrate the Monte Carlo sampling procedure with a simple example.

[25] Figure 3a shows the results of the random walk process that generates candidate GPTSs. The sampling starts from an arbitrary GPTS constructed by concatenating polarity chron durations sampled from the prior distribution. We use here a lognormal prior distribution for the polarity chron durations with a mean and variance taken from the log-chron durations in previous M-sequence GPTSs (CENT94, GTS2004, and TS10). Ages in the GPTS are then rescaled to match dates sampled from the normal distribution that defines the uncertainty of the two radiometric dates used here (for clarity of illustration, these dates are fixed to their mean value in the example of Figure 3). The random walk modifies iteratively this initial GPTS by choosing one chron at random, sampling a new duration for this chron from the prior distribution, and rescaling the GPTS to match new values for radiometric dates sampled from their distribution. Repeating this random walk process generates an ensemble of GPTSs that match radiometric dates within their uncertainty and have a broad distribution of polarity chron durations.

[26] Figure 3b shows the result of accepting or rejecting candidate GPTSs generated by the previous random walk algorithm depending on how much they minimize the global variation of spreading rates. The probability of accepting a candidate depends on the likelihood function of spreading rates $p(\mathbf{b} \mid \mathbf{m})$, defined in Appendix A. An important parameter in this likelihood is a measure of how much the spreading rates in each block are expected to fluctuate. As the lineation sets considered here have markedly different spreading rates, we quantify the spreading rate variation with a global coefficient of variation (CV), the standard deviation of spreading rates divided by their average. In practice, it is impossible to obtain a GPTS that makes spreading rates constant in all the block models, and we determined a target value for the CV by running sampling experiments and observing how much the variation of spreading rates can be actually minimized. We found sampling could reduce the global CV to about 50% at best, and we use this value for the likelihood function in our final simulation. This value is confirmed by an analysis of the CV expected for estimated errors in the block model distances, asymmetric spreading, and long-term variations in spreading rate (Appendix B).

[27] The sampling results in Figure 3b are clearly different from those in Figure 3a. Rather than fluctuating erratically throughout, the sampled GPTSs in Figure 3b progressively adjust to minimize spreading rate variations during a "burn-in" phase that lasts a couple of thousand iterations and then display changes much smaller than those in Figure 3a. After the "burn-in" phase, the ensemble of GPTSs in Figure 3b will have a distribution defined by the product $p(\mathbf{m})\, p(\mathbf{d} \mid \mathbf{m})\, p(\mathbf{b} \mid \mathbf{m})$ of equation (1), the prior times the likelihoods of the radiometric dates **d** and of the spreading rates given by the block model distances in **b**.

[28] Finally, Figure 3c shows the result of including the likelihood function $p(\mathbf{c} \mid \mathbf{m})$ of polarity chron durations from astrochronology, defined in Appendix A. Astrochronologies constrain the youngest five polarity chrons in the M-sequence GPTS (Table 2), and Figure 3c shows that the variation in the duration of these chrons is reduced compared to Figure 3b. After the "burn-in" phase, the ensemble of GPTSs in Figure 3c will be distributed as in the full posterior distribution of equation (1) and will simultaneously agree with radiometric dates, minimize the global variation of spreading rates, and fit polarity chron duration constraints.

5. Application to the CENT94 Block Models

[29] To demonstrate how the Monte Carlo sampling method minimizes global spreading rate variations, we applied it to the Hawaii, Japanese, Phoenix, and Keathley block model distances in CENT94. The CENT94 GPTS was built assuming constant spreading rates in the Hawaiian lineations, and it results in variable spreading rates in the other block models (CV of 45–56%; Figure 4a). We computed an alternative GPTS by running the Monte Carlo sampling method with the polarity block models and absolute age constraints used in CENT94. The resulting GPTS allows for some variability of spreading rates in the Hawaii block model (CV = 24%; Figure 4b), but the rate fluctuations in the other three block models are smaller compared to CENT94. In the Japanese and

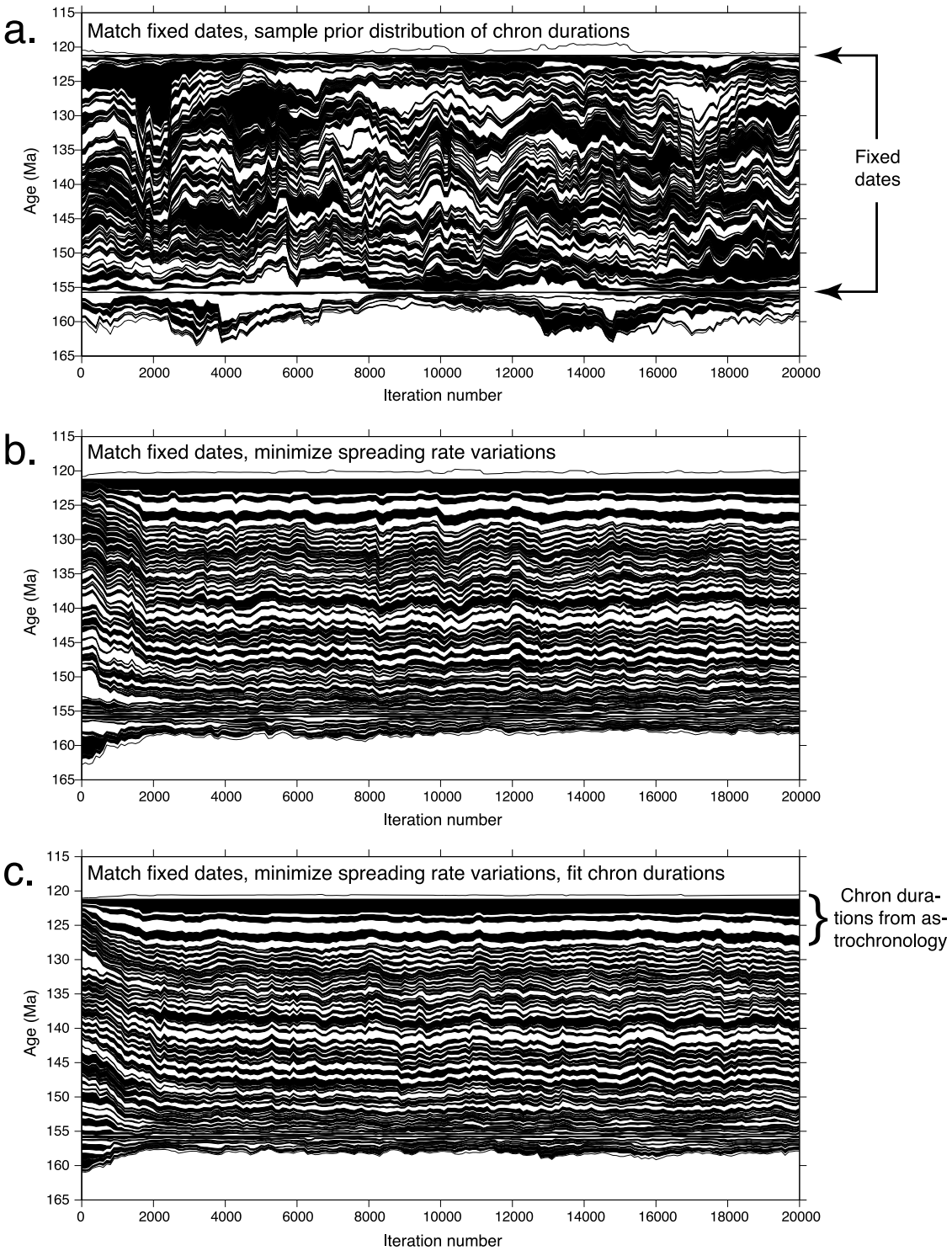

Figure 3. Illustrative Monte Carlo sampling of M-sequence GPTSs for different constraints. Each sampled GPTS is plotted in the usual convention (black is normal polarity, white is reversed). (a) The algorithm generates candidate GPTSs whose chron durations are distributed as in the prior distribution and that match two radiometric dates. The two dates (121.2 Ma and 155.3 Ma) are fixed for clarity in this illustration. (b) Candidate GPTSs that minimize spreading rate variations are preferentially accepted. (c) In addition to minimizing spreading rate variations, the GPTSs are also constrained by the durations estimated by astrochronology of the five youngest polarity chrons.

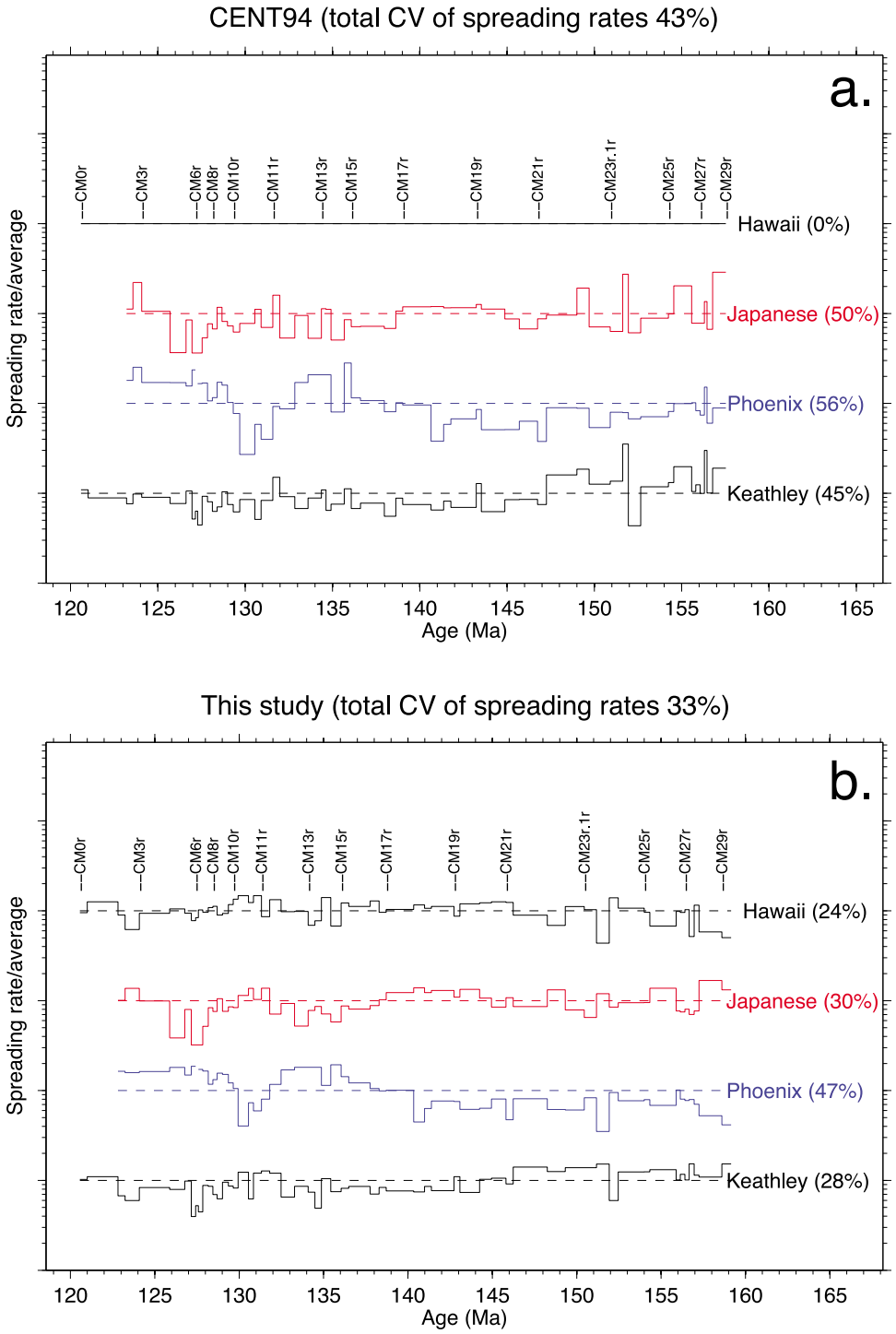

Figure 4. (a) Spreading rates implied by the CENT94 GPTS in the block models of *Channell et al.* [1995]. CENT94 was built assuming constant spreading rates in the Hawaiian block model. Percentages in parentheses indicate the coefficient of variation (CV = standard deviation/average) of spreading rate in each block model. (b) A time scale obtained by applying the Monte Carlo method described here minimizes spreading rate fluctuations in all the block models.

Keathley block models, the CV of spreading rates decreases to 28–30%, a value comparable to that in the Hawaii block model. As in the results of *Channell et al.* [1995], the Phoenix lineations display the most variable spreading rates (CV = 47%). The alternative GPTS also attenuates some prominent spreading rate spikes (e.g., in CM24 of the Japanese and Keathley block models). The total CV of spreading rates, which was 43% in CENT94, is reduced to 33%. Age

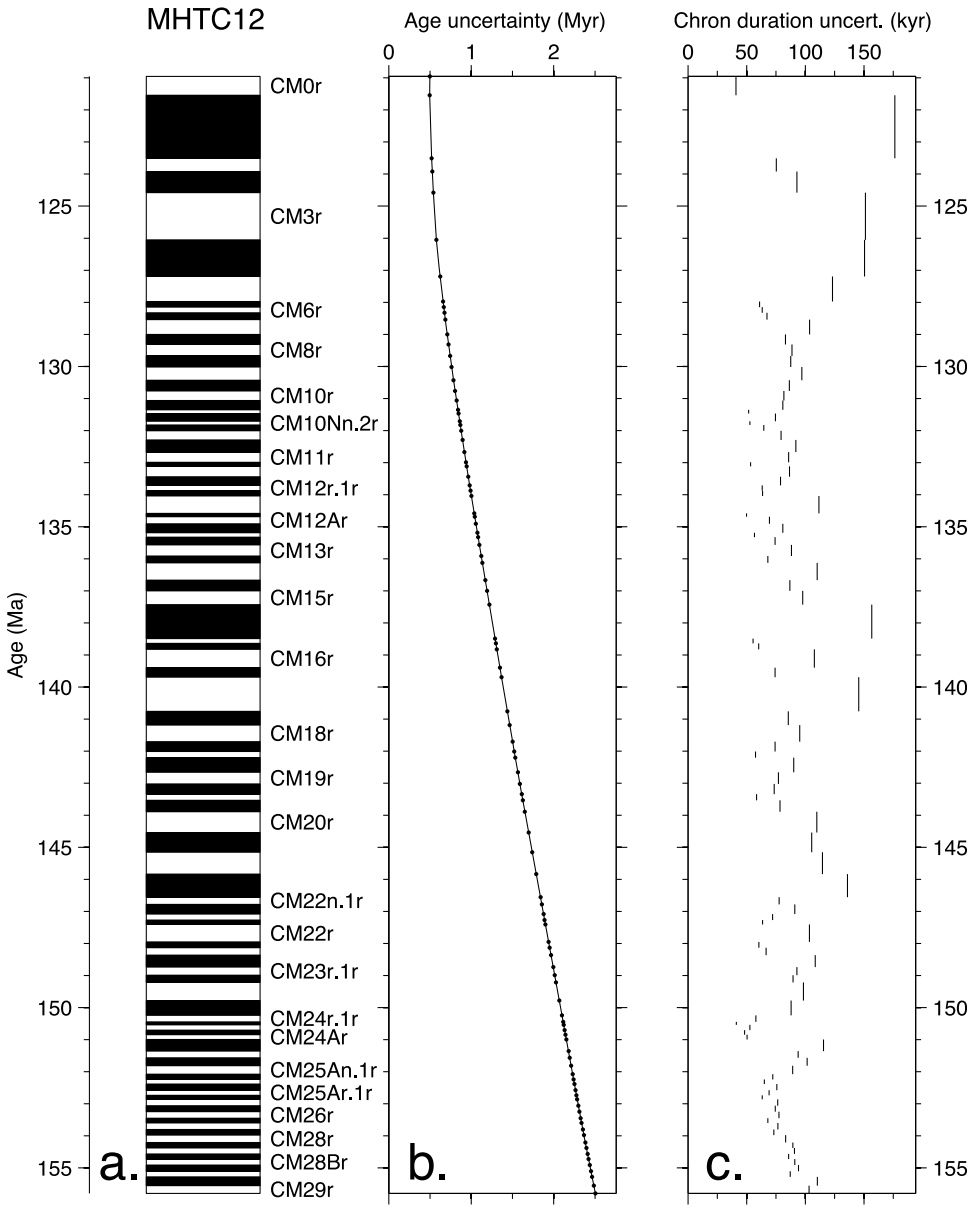

Figure 5. (a) MHTC12 is the average M-sequence GPTS in the Monte Carlo simulation. (b) The associated uncertainties in the ages of chron boundaries and (c) the chron duration uncertainties. Uncertainties are one standard deviation.

differences between CENT94 and the alternative GPTS are not insignificant, reaching ~400 kyr around CM1 and CM10 and ~800 kyr around CM22.

[30] This alternative GPTS demonstrates that the Monte Carlo method can reduce the variability of spreading rates on multiple block models from several spreading centers. The rest of this paper describes the new MHTC12 GPTS we obtain by minimizing spreading rate fluctuations for the TS10 polarity block models.

6. The MHTC12 M-Sequence GPTS and Its Uncertainty

[31] MHTC12 is shown in Figure 5 and listed in Table 3. The MHTC12 ages are the average of the ensemble of GPTSs generated by Monte Carlo sampling, and the uncertainties in ages of chron boundaries and chron durations are the standard deviations of the ensemble. The age uncertainties we calculate are close to those reported by *Hinnov and Ogg* [2007], who estimated a 95% confidence limit (two standard deviations) of 4 Myr in the Upper Jurassic interval of the M-sequence (approximately CM29-CM19), decreasing in the Cretaceous to 1 Myr around CM0r. The ages and uncertainties in Table 3 are also included in the auxiliary material, together with results for an alternative MHTC12–125 obtained in the same way except for an age of 125 ± 0.5 Ma assigned to the onset of CM0r (see the "Radiometric dates" section). Details on the sampling procedure are in Appendix A.

[32] Figure 6 compares the variability in spreading rates for MHTC12 to that of TS10. TS10 was constructed by

Table 3. MHTC12 M-Sequence GPTS and Estimated Uncertainties[a]

Polarity Chron	End Age (Ma)	End Age Uncertainty (Myr)	Duration Uncertainty (Myr)
CM0r	120.95	0.498	0.0409
CM1n	121.54	0.497	0.176
CM1r	123.51	0.52	0.0753
CM3n	123.92	0.528	0.0929
CM3r	124.58	0.542	0.151
CM5n	126.05	0.577	0.15
CM5r	127.19	0.623	0.123
CM6n	127.98	0.658	0.061
CM6r	128.15	0.666	0.0632
CM7n	128.33	0.675	0.0673
CM7r	128.54	0.686	0.104
CM8n	129	0.709	0.0831
CM8r	129.32	0.726	0.0886
CM9n	129.67	0.744	0.0876
CM9r	130.02	0.762	0.0971
CM10n	130.43	0.786	0.0864
CM10r	130.76	0.804	0.0817
CM10Nn.1n	131.07	0.822	0.0808
CM10Nn.1r	131.35	0.839	0.0517
CM10Nn.2n	131.47	0.846	0.0745
CM10Nn.2r	131.71	0.861	0.0528
CM10Nn.3n	131.83	0.867	0.0647
CM10Nr	132.01	0.878	0.0793
CM11n	132.3	0.895	0.092
CM11r	132.67	0.917	0.0857
CM11An	132.99	0.937	0.0534
CM11Ar	133.12	0.945	0.0865
CM12n	133.44	0.965	0.0788
CM12r.1r	133.71	0.982	0.0632
CM12r.1n	133.88	0.992	0.0635
CM12r.2r	134.04	1	0.112
CM12An	134.58	1.04	0.0498
CM12Ar	134.69	1.04	0.0695
CM13n.1n	134.91	1.06	0.0809
CM13n.1r	135.19	1.07	0.0567
CM13n.2n	135.33	1.08	0.0742
CM13r	135.56	1.1	0.0882
CM14n	135.92	1.12	0.0681
CM14r	136.13	1.14	0.11
CM15n	136.66	1.17	0.0868
CM15r	137	1.19	0.0977
CM16n	137.43	1.22	0.157
CM16n.1r	138.49	1.29	0.0555
CM16n.2n	138.64	1.3	0.0602
CM16r	138.82	1.31	0.108
CM17n	139.4	1.35	0.0743
CM17r	139.69	1.37	0.145
CM18n	140.76	1.44	0.0854
CM18r	141.19	1.47	0.0952
CM19n.1n	141.7	1.5	0.0743
CM19n.1r	142.01	1.52	0.0576
CM19n.2n	142.2	1.53	0.0901
CM19r	142.66	1.57	0.0771
CM20n.1n	143.02	1.59	0.0735
CM20n.1r	143.34	1.61	0.0585
CM20n.2n	143.53	1.63	0.0784
CM20r	143.89	1.65	0.11
CM21n	144.54	1.7	0.105
CM21r	145.16	1.74	0.115
CM22n.1n	145.83	1.79	0.136
CM22n.1r	146.56	1.84	0.0777
CM22n.2n	146.78	1.86	0.091
CM22n.2r	147.08	1.88	0.0721
CM22n.3n	147.27	1.89	0.0635
CM22r	147.41	1.9	0.103
CM22An	147.95	1.94	0.0604
CM22Ar	148.13	1.95	0.0665
CM23n	148.36	1.97	0.108
CM23r.1r	148.74	2	0.0928
CM23r.1n	148.99	2.01	0.0895
CM23r.2r	149.21	2.03	0.0985
CM24n	149.78	2.07	0.0879
CM24r.1r	150.24	2.1	0.0579
CM24r.1n	150.44	2.11	0.0413
CM24r.2r	150.54	2.12	0.0528
CM24An	150.7	2.13	0.0483
CM24Ar	150.84	2.14	0.0503
CM25n	150.99	2.15	0.115
CM25r	151.36	2.18	0.0939
CM25An.1n	151.56	2.19	0.102
CM25An.1r	151.81	2.21	0.0892
CM25An.2n	152.07	2.23	0.0722
CM25An.2r	152.24	2.24	0.0651
CM25An.3n	152.38	2.25	0.0757
CM25Ar.1r	152.58	2.26	0.0692
CM25Ar.1n	152.73	2.27	0.0633
CM25Ar.2r	152.86	2.28	0.0765
CM26n	153.06	2.3	0.0743
CM26r	153.25	2.31	0.0775
CM27n	153.45	2.33	0.0681
CM27r	153.6	2.34	0.0767
CM28n	153.8	2.35	0.0732
CM28r	153.98	2.37	0.0833
CM28An	154.21	2.38	0.0894
CM28Ar	154.38	2.4	0.0907
CM28Bn	154.56	2.41	0.0858
CM28Br	154.72	2.42	0.0911
CM28Cn	154.91	2.44	0.0942
CM28Cr	155.11	2.45	0.0872
CM29n	155.28	2.46	0.11
CM29r	155.55	2.49	0.103
CM30n	155.79	2.51	

[a]Uncertainties are one standard deviation. Polarity chron nomenclature is as in TS10, with CM25Ar, CM25n5, and CM25r5 in TS10 changed to CM25Ar.1r, CM25Ar.1n, and CM25Ar.2r, respectively, to follow general chron nomenclature rules.

minimizing spreading rate variations in the Pacific lineations (Hawaii, Japanese, and Phoenix), and as expected it results in a lower CV of spreading rates for the Pacific block models compared to those in the Indian and Atlantic Ocean (Figure 6a). At the price of a small increase in the CV of the Pacific lineations, MHTC12 decreases spreading rate fluctuations in the Indian and Atlantic Ocean block models, making the CV of spreading rates in different block models more uniform (Figure 6b). Also, the total CV of spreading rates decreases from 51% in TS10 to 44% in MHTC12. While this is not a dramatic improvement, the CV of measured spreading rates is not expected to be much less than 50% (Appendix B), and the addition of information from the Indian and Atlantic Ocean block models improves the reliability of MHTC12.

[33] Figure 7 compares histograms of the youngest five polarity chron durations in the MHTC12 ensemble with the means and standard deviations given by astrochronology (Table 2). Although the astrochronology data were taken into account during the sampling, the distributions of sampled chron durations do not exactly match those given by astrochronology. The reason is that the sampled chron durations do not only have to fit the astrochronology data, but also need to minimize spreading rate variations. Each of these pieces of information influences the sampling process, and their respective weights depend on the uncertainty of the astrochronology data and on the CV of spreading rates. This

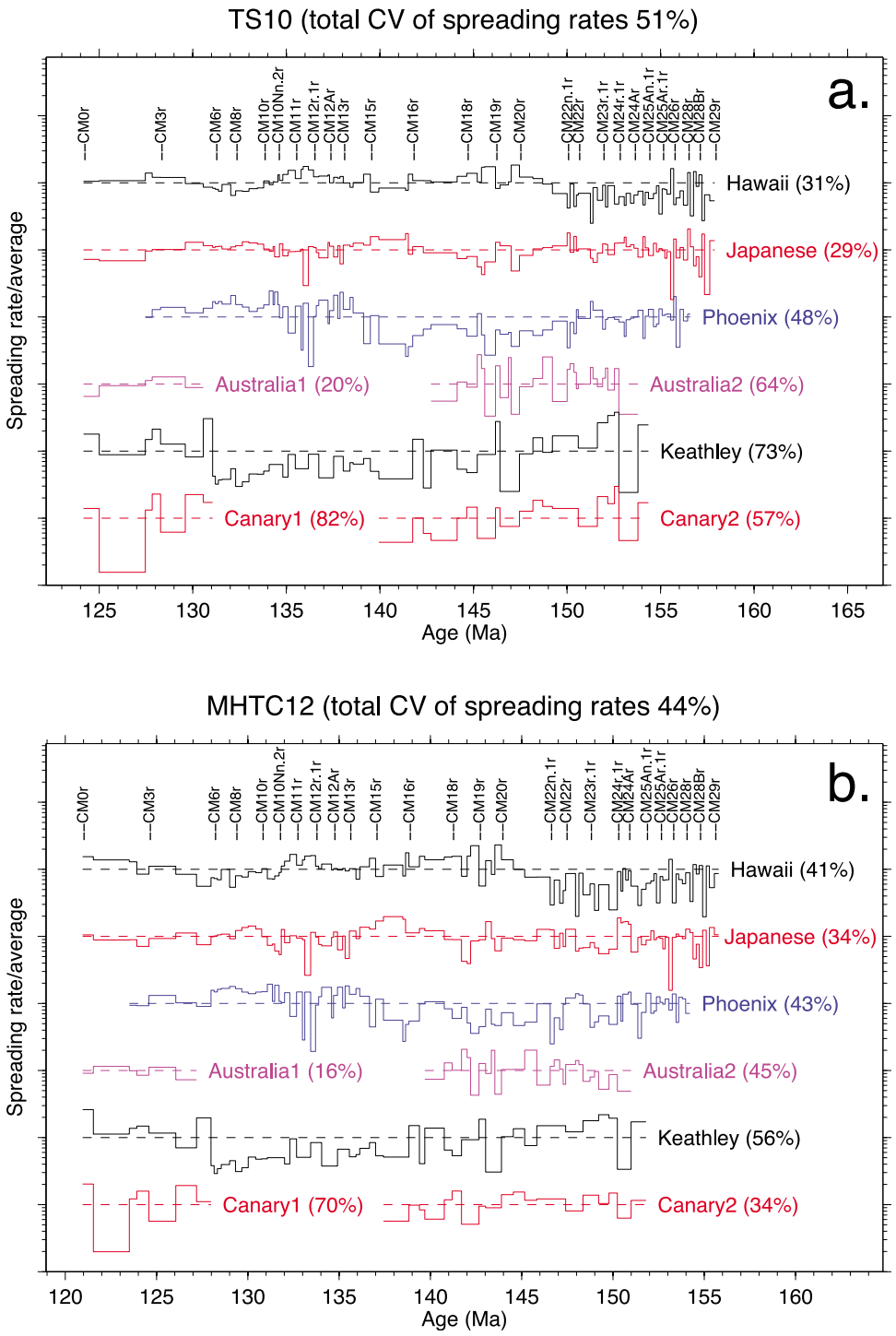

Figure 6. Spreading rates implied by the (a) TS10 GPTS and (b) MHTC12. Percentages in parentheses indicate the coefficient of variation (CV = standard deviation/average) of spreading rate in each block model. The TS10 GPTS results in lower CVs for the block models that were used to construct the time scale (Hawaii, Japanese and Phoenix) compared to those of block models from other spreading centers. The GPTS obtained here, which uses all block models, decreases the total CV of spreading rates (44% versus 51% for TS10) and the differences between the CVs of different block models.

comparison underscores an important point: when different kinds of data are included in the GPTS construction, the final GPTS will not necessarily match exactly each piece of information.

[34] This point is further illustrated in Figure 8, where the ages in the MHTC12 ensemble for the middle of CM0r and the end of CM26n are compared with the means and standard deviations of the corresponding radiometric dates (see the

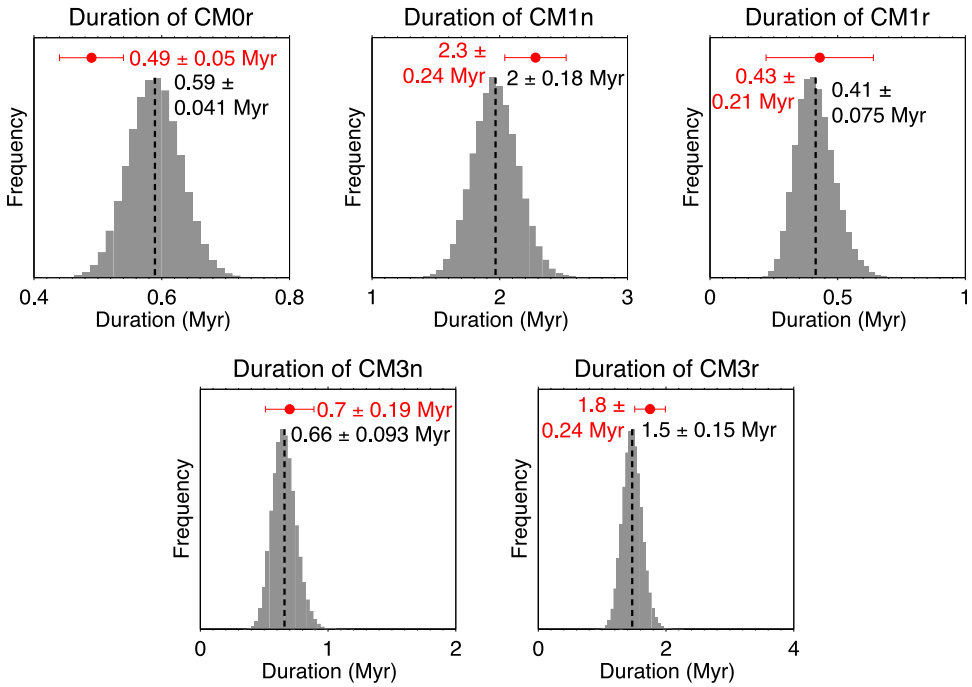

Figure 7. Chron durations in MHTC12 (gray histograms, average and standard deviation in black lettering) compared to chron duration estimates from astrochronology used in constructing the time scale (mean and standard deviation in red symbols and letters). The sampled chron durations do not match exactly the uncertainties of the astrochronology estimates because the sampled GPTSs also need to minimize the total variability of spreading rates.

"Radiometric dates" section). While the distributions are the same for CM0r, they differ somewhat for CM26n, whose radiometric age has a large uncertainty of 3.4 Myr. This difference is slight: more than 95% of the ages sampled in the MHTC ensemble for CM26n are within the 95% bounds of the radiometric age (±two standard deviations). The reason for this difference is that the polarity chron durations from astrochronology place a weak constraint on the average spreading rates. This constraint propagates to the older end of the GPTS, resulting in an average age in the sampled ensemble that is slightly younger and has a smaller uncertainty than the radiometric date. This explanation has been tested by running the Monte Carlo simulation without the chron durations from astrochronology; in this case, the sampled age distribution of CM26n matches that of the corresponding radiometric age (actual results not shown).

[35] MHTC12 is constrained only by two radiometric dates, and Figure 9 compares the sampling results to the other dates listed in Table 1. The comparison in Figure 9 excludes the 125 ± 0.5 Ma age assigned to the onset of CM0r by

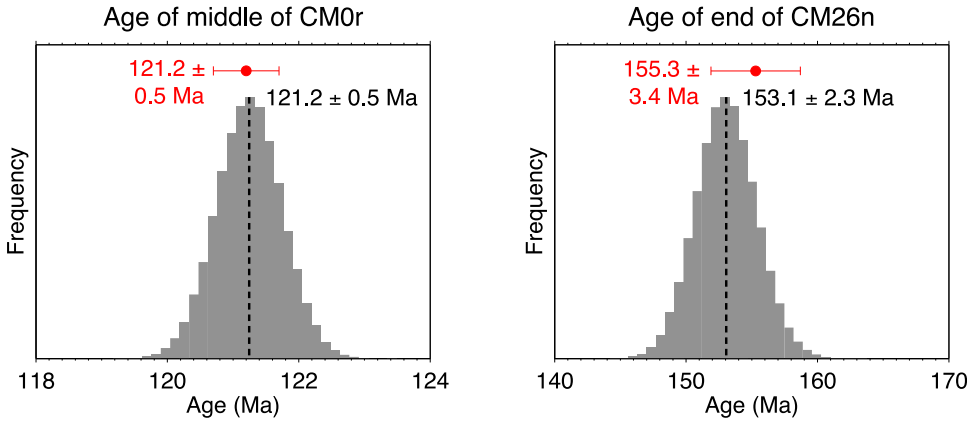

Figure 8. Ages in MHTC12 (gray histograms, average and standard deviation in black lettering) compared to radiometric dates used in constructing the time scale (mean and standard deviation in red symbols and letters). The age of CM26n does not match exactly the uncertainty of the corresponding radiometric date because the chron durations from astrochronology constrain the average spreading rates.

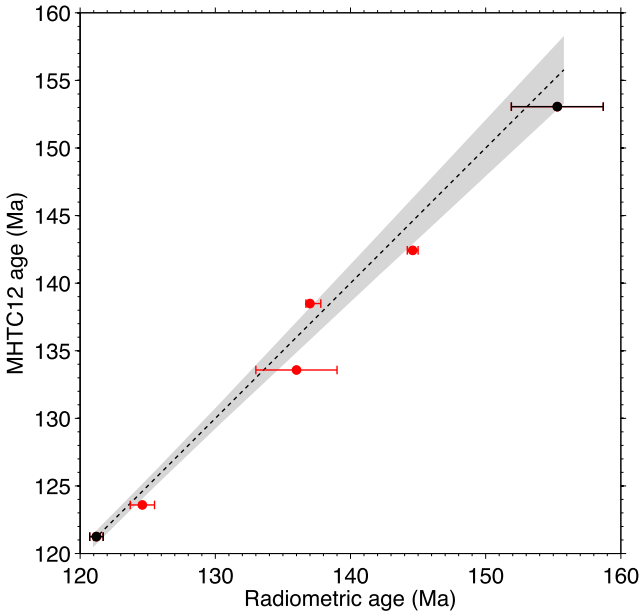

Figure 9. Comparison between ages in the sampled GPTSs and radiometric dates from Table 1. The dashed line marks equal ages, the gray region shows the uncertainty of MHTC12, and the error bars denote the uncertainties of the measured dates (uncertainties are ± one standard deviation). MHTC12 was constrained only by the two dates shown in black. Radiometric dates that were not used in constructing the GPTS, shown in red, generally agree with MHTC12 given the respective uncertainties.

GTS2004, which is an alternative interpretation (see the "Radiometric dates" section). The sampled GPTS ages are consistent with all the radiometric dates, given the respective uncertainties. We note that the uncertainties in Figure 9 for the dates not used in constraining the GPTS are minimum values, because they represent analytical errors only and do not include uncertainties due to approximate correlations to the polarity reversal record. For example, the 137 Ma date of *Bralower et al.* [1990] has been assigned to the middle of the CM16n-CM16r interval in Figure 9; this date, however, could correspond to any point in this interval, which spans almost 2 Myr.

[36] Figure 10 compares MHTC12 ages to previous M-sequence GPTSs. MHTC12 is our preferred time scale, but to make a fair comparison Figure 10 shows differences with MHTC12–125 for GTS2004 and TS10, which assumed an age of 125 Ma for the onset of CM0r. Some of the differences with CENT94 and GTS2004 (e.g., in the interval CM10N-CM14) are likely due to the different polarity block models used to build these GPTSs. Age differences with TS10 are smoother, as TS10 was based on the same Pacific block models, but they still can exceed 1 Myr (e.g., around CM20). While MHTC12 is an important update of the M-sequence GPTS, it is sobering to note that age differences with previous time scales are within two standard deviations of the uncertainty inherent to MHTC12 (Figure 10). Improving the accuracy of the M-sequence time scale will require more absolute age constraints and chron duration estimates from astrochronology. As new data become available, the time scale can be easily updated by repeating the Monte Carlo sampling procedure.

[37] Using the correlations of polarity chrons to geologic stage boundaries of *Channell et al.* [1995, 2010], MHTC12 leads to the following stage boundary ages: Oxfordian/Kimmeridgian at ~151.3 Ma, Kimmeridgian/Tithonian at 148.0 Ma, Jurassic/Cretaceous at 141.7 Ma, Berriasian/Valanginian at 136.8 Ma, Valanginian/Hauterivian at 132.7 Ma, Hauterivian/Barremian at ~126 Ma, and Barremian/Aptian at 121.54 Ma.

7. Conclusions

[38] Geomagnetic polarity time scales (GPTSs) are currently constructed from magnetic anomaly lineations by assuming nearly uniform spreading rates over time at one or a few selected spreading centers. A drawback of this procedure is that spreading rates at other mid-ocean ridges will vary more erratically, whereas an optimal GPTS should minimize the variation of spreading rates at as many spreading centers as possible. This need is underscored by astrochronology-based GPTSs obtained for the last few Ma, which result in smaller spreading rate fluctuations compared to those implied by GPTSs constructed from marine magnetic anomalies.

[39] We describe a Monte Carlo method that improves GPTS construction by minimizing spreading rate variations in a global data set and by also incorporating information on chron durations estimated from astrochronology. We apply the method to construct a new version of the Late Jurassic-Early Cretaceous M-sequence GPTS based on magnetic lineations from the Western Pacific, North Atlantic, and Indian Ocean NW of Australia. This MHTC12 GPTS also accounts for the duration of five polarity chrons (CM0r through CM3r) established from astrochronology studies of Cretaceous sedimentary sequences. Absolute ages are constrained by two radiometric dates, 121.2 ± 0.5 Ma for the middle of CM0r and 155.3 ± 3.4 Ma for the end of CM26n. While MHTC12 is our preferred time scale, the CM0r date is debated, and we include in the auxiliary material an alternative GPTS (MHTC12–125) constructed with an onset of CM0r at 125 ± 0.5 Ma.

[40] The Monte Carlo sampling procedure generates a large ensemble of GPTSs that simultaneously agree with radiometric age constraints, minimize the total variation of spreading rates, and fit polarity chron durations estimated by astrochronology. The average and standard deviation of this ensemble provide a reference time scale and its uncertainty, respectively. A key feature of this approach is that it accounts for and propagates the uncertainties of the input data, which weigh how much each piece of information constrains the time scale.

[41] MHTC12 reduces the global variability of spreading rates compared to a previous GPTS based on the Western Pacific lineations only, fits radiometric date and astrochronology data within their uncertainties, and is in broad agreement with other radiometric dates that were not used to constrain the solution. An added benefit of this procedure is that it is fully automated, so that the time scale can be easily updated by repeating the Monte Carlo sampling with future data additions (magnetic block model distances, radiometric dates, or polarity chron duration estimates from astrochronology).

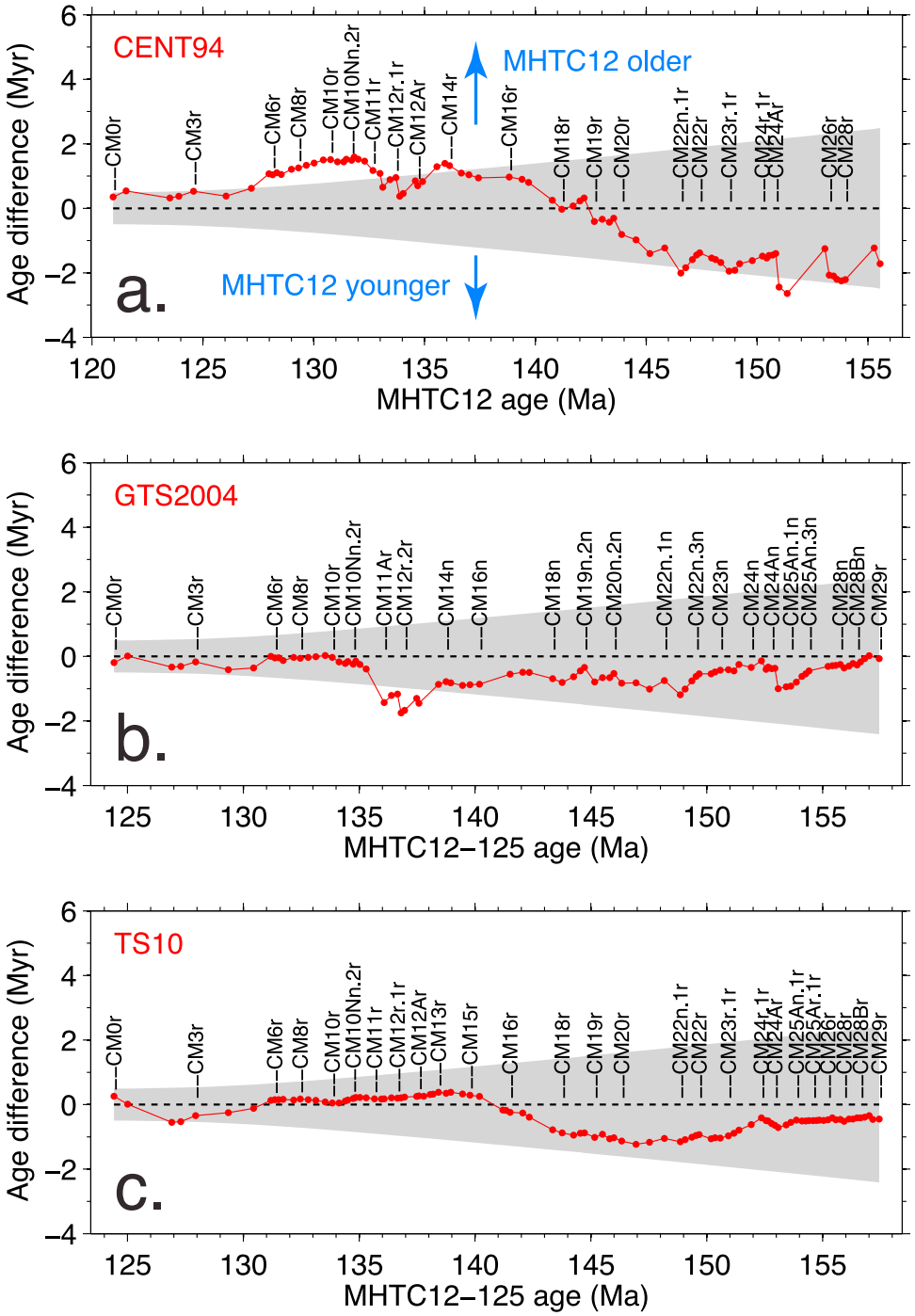

Figure 10. Comparison between ages in MHTC12 and ages in (a) CENT94, (b) GTS2004, and (c) TS10. Age differences on the vertical axes are ages in MHTC12 minus ages in the other time scale. The dashed line marks zero age difference and the gray region shows the uncertainty in MHTC12 (±one standard deviation).

Appendix A: Markov Chain Monte Carlo Algorithm

A1. Likelihood of Block Model Distance Data

[42] This likelihood function minimizes the total variation of spreading rates: for block model distances in a vector **b**, the likelihood is higher if the total variation of spreading rates implied by the GPTS in vector **m** is smaller. The likelihood is

$$p(\mathbf{b}|\mathbf{m}) = \text{const.} \times \exp\left\{\frac{\sum_{i=1}^{B} N_i}{\sum_{i=1}^{B} T_i} \sum_{i=1}^{B} \left[-\frac{1}{2(v\mu_i)^2} \sum_{j=1}^{N_i} (u_{ij} - \mu_i)^2 \Delta t_{ij}\right]\right\}, \quad \text{(A1)}$$

where B is total number of block models, N_i is number of blocks in i-th block model, T_i is total duration of i-th block model, as in

$$T_i = \sum_{j=1}^{N_i} \Delta t_{ij,} \tag{A2}$$

where Δt_{ij} is duration of j-th chron of the i-th block model (from GPTS in $\mathbf{m}$), u_{ij} is spreading rate of j-th block in i-th block model, as in

$$u_{ij} = \frac{\Delta x_{ij}}{\Delta t_{ij}}, \tag{A3}$$

where Δx_{ij} is width of j-th block in i-th block model (from distances in $\mathbf{b}$), v is coefficient of variation (CV) of spreading rates (see the text and Appendix B), and μ_i is average spreading rate in i-th block model, weighted by chron duration as in

$$\mu_i = \frac{1}{T_i} \sum_{j=1}^{N_i} u_{ij} \Delta t_{ij} = \frac{1}{T_i} \sum_{j=1}^{N_i} \Delta x_{ij}. \tag{A4}$$

The likelihood in (A1) is weighted by polarity chron duration, so that a given difference from the average spreading rate in a longer chron decreases the likelihood more than the same difference in a shorter chron.

A2. Likelihood of Chron Duration Data

[43] This likelihood function is higher if the polarity chron durations implied by the GPTS in vector $\mathbf{m}$ are closer to the chron duration estimates in a vector $\mathbf{c}$. The likelihood is

$$p(\mathbf{c} \mid \mathbf{m}) = \text{const.} \times \exp\left[- \sum_{j=1}^{C} \frac{\left(c_j - \Delta t_j\right)^2}{2\sigma_j^2} \right], \tag{A5}$$

where C is total number of chron durations from astrochronology, c_j is mean of j-th chron duration (from astrochronology data in $\mathbf{c}$), σ_j is standard deviation of j-th chron duration, and Δt_j is duration of j-th chron (from GPTS in $\mathbf{m}$).

A3. MCMC Sampling Algorithm

[44] The MCMC algorithm used to generate samples from the posterior distribution of GPTS vectors $\mathbf{m}$ in equation (1) starts from a random initial GPTS constructed in two steps. First, a random GPTS vector $\mathbf{m}$ is constructed by concatenating the desired number of chron durations sampled from their prior distribution (see Section 4). The chron ages in $\mathbf{m}$ are then rescaled to match values for the absolute dates that were sampled from the distributions that define the uncertainty of radiometric dates. Sampling then proceeds as follows:

[45] 1. Generate a candidate GPTS in a vector $\mathbf{m}_{\text{cand}}$ by (a) picking at random a chron in $\mathbf{m}$ and perturbing its duration (these perturbations are designed to sample the prior distribution of chron durations) and (b) rescaling the ages in $\mathbf{m}_{\text{cand}}$ to match dates sampled from the distribution of radiometric dates.

[46] 2. Accept the candidate GPTS with a probability equal to the ratio of the likelihoods as in

$$\alpha = \min\left[1, \frac{p(\mathbf{b}|\mathbf{m}_{\text{cand}})}{p(\mathbf{b}|\mathbf{m})} \times \frac{p(\mathbf{c}|\mathbf{m}_{\text{cand}})}{p(\mathbf{c}|\mathbf{m})}\right]. \tag{A6}$$

In practice, generate a random number r from a uniform distribution between 0 and 1. If $r < \alpha$, set $\mathbf{m} = \mathbf{m}_{\text{cand}}$; otherwise, leave $\mathbf{m}$ unchanged. Note that α depends only on the ratio of the likelihoods, so that the constants in equations (A1) and (A5) are irrelevant.

[47] 3. Every 100 iterations, save the current value of $\mathbf{m}$.

[48] 4. Repeat from step 1.

[49] The ensemble used to obtain the final GPTS (Figure 5, Table 3, and supplementary material) was obtained by combining 500 independent chains started from different random initial GPTSs. This strategy ensures that the starting point does not affect the solution. The final variability of the sampled GPTSs is much less than the differences between the starting GPTSs, indicating that the chains were not trapped in secondary modes and that they converged to sample the global mode of the posterior distribution. The histograms of sampled chron ages and durations (Figures 7 and 8) do not show any sign of multimodality. Each chain was run for 50,000 iterations, and to safely discard the burn-in interval, the first 10,000 iterations in each chain were ignored. The sampling algorithm saves only one GPTS every 100 iterations (see step 4 above). This is done to reduce the redundancy of the samples: consecutive samples are very similar because only one chron is changed for each iteration. The interval between saved samples is close to the number of chrons in the M-sequence (102). The final ensemble consisted of 200,000 GPTSs. The convergence of the simulation was assessed by comparing the statistics of the two halves of the ensemble. The average ages of the polarity chron boundaries in each half were very close, with differences that were at most $\sim$1% of the standard deviation. Again, this close comparison confirms that the independent chains were sampling the global mode of the posterior distribution.

Appendix B: CV of Spreading Rates

[50] The likelihood of block model distance data, which quantifies the total variation of spreading rates (equation (A1)), needs a value for v, the coefficient of variation (CV) of spreading rates. To estimate an expected CV in the set of block model distances used here, we consider three reasons for measured spreading rates to depart from a constant value.

[51] *Errors in measured model block widths.* The spreading rate calculated in a given polarity block equals the block width divided by the duration of the polarity chron. For a given chron duration, an error in the measured block width directly translates into an error in the calculated spreading rate, so that the CV of the spreading rates equals the CV of the block widths. We use here the polarity block distance data published by TS10, who estimated block model uncertainties by comparing multiple magnetic anomaly profiles. TS10 report standard deviations of the polarity block widths in the Western Pacific as 2–36 km (average 11 km) for Hawaii, 1–36 km (14 km) for the Japanese, and 2–33 km (9 km) for the Phoenix model. The average standard deviations are large compared to the average

block widths (19.4, 19.7, and 11.2 km in the Hawaii, Japanese, and Phoenix block models, respectively), and these averages are likely biased by a few large standard deviations. We obtained an alternative estimate of the standard deviations of the block widths from the standard deviations of the block model distances listed by TS10. To deduce the errors in block widths from those of the distances, consider a simple case where the blocks are referred to a common origin so that the distance to a polarity block boundary is the sum of all the preceding block widths. Assuming that errors in block widths are uncorrelated, the variances of the distances are expected to grow from the origin, and the average increase in variance per block is the average variance of block widths. In the TS10 data, the expected increase of variance is not observed in the Western Pacific because several intervals with different origins were used to construct composite block models. In the Atlantic Keathley lineations, however, there is a clear linear increase in the variance of the distances that averages 31.6 km^2 per block, giving a standard deviation for the block widths of 5.6 km. When divided by the average block width of 12 km, this gives a CV of 0.47 for the block widths and for the spreading rates estimated in this block model. Using the same standard deviation for the block widths in the Western Pacific Hawaii lineations (average block width 19.4 km) gives a CV of 0.29 for the spreading rates. The average of the Atlantic and Pacific CVs is 0.38.

[52] *Asymmetric spreading.* In block models constructed from a single ridge flank, asymmetric spreading during a polarity chron will result in a variation of measured spreading rate. The Keathley and Canary block models are from conjugate ridge flanks, and averaging their distances would remove the effect of asymmetric spreading. As all other block models in our data set are from a single ridge flank, however, we could not eliminate this cause of spreading rate variability and opted not to average the Keathley and Canary block model distances. A histogram of spreading asymmetries from the global survey of *Müller et al.* [2008] gives a CV of 10/50 = 0.2 for spreading rate fluctuations due to asymmetries.

[53] *Long-term variations in spreading rate.* The best-studied C-sequence magnetic anomaly corridor in the South Atlantic shows long-term variations in spreading rate [*Cande and Kent*, 1995]. This long-term variation, as summarized in *Ogg and Smith* [2004, Figure 5.3], is consistent with a CV of 5/22.5 = 0.22.

[54] The total CV of spreading rates due to these three causes is the square root of the sum of the variances and comes to 0.48, or about 50%.

[55] **Acknowledgments.** A.M. and J.H. were supported by NSF grant OCE 09–26306, M.T. was supported by a Woods Hole Oceanographic Institution postdoctoral scholarship, and J.E.T.C. was supported by NSF grant OCE 09–60999. Thanks to two anonymous reviewers for comments that improved the manuscript. Figure 1 was constructed with the GMT software of *Wessel and Smith* [1991]. This is LDEO contribution number 7551.

References

Acton, G. D., and S. P. Huestis (1994), Genetic algorithm optimization for seafloor spreading rates and geomagnetic polarity time scales, *Eos Trans. AGU*, *75*(44), Fall Meet. Suppl., Abstract GP42B-14.

Agrinier, P., Y. Gallet, and E. Lewin (1999), On the age calibration of the geomagnetic polarity timescale, *Geophys. J. Int.*, *137*, 81–90, doi:10.1046/j.1365-246x.1999.00755.x.

Baksi, A. K. (1994), Concordant sea-floor spreading rates obtained from geochronology, astrochronology and space geodesy, *Geophys. Res. Lett.*, *21*, 133–136, doi:10.1029/93GL03534.

Berger, A., M. F. Loutre, and J. Laskar (1992), Stability of the astronomical frequencies over the Earth's history for paleoclimate studies, *Science*, *255*, 560–566, doi:10.1126/science.255.5044.560.

Billups, K., H. Pälike, J. E. T. Channell, J. C. Zachos, and N. J. Shackleton (2004), Astronomic calibration of the Late Oligocene through Early Miocene geomagnetic polarity time scales, *Earth Planet. Sci. Lett.*, *224*, 33–44, doi:10.1016/j.epsl.2004.05.004.

Bralower, T. J., K. R. Ludwig, J. D. Obradovich, and D. L. Jones (1990), Berriasian (Early Cretaceous) radiometric ages from the Grindstone Creek Section, Sacramento Valley, California, *Earth Planet. Sci. Lett.*, *98*, 62–73, doi:10.1016/0012-821X(90)90088-F.

Cande, S. C., and D. V. Kent (1992), A new geomagnetic polarity time scale for the Late Cretaceous and Cenozoic, *J. Geophys. Res.*, *97*(B10), 13,917–13,951, doi:10.1029/92JB01202.

Cande, S. C., and D. V. Kent (1995), Revised calibration of the geomagnetic polarity time scale for the Late Cretaceous and Cenozoic, *J. Geophys. Res.*, *100*(B4), 6093–6095, doi:10.1029/94JB03098.

Channell, J. E. T., E. Erba, M. Nakanishi, and K. Tamaki (1995), Late Jurassic-Early Cretaceous time scales and oceanic magnetic anomaly block models, in *Geochronology, Timescales, and Stratigraphic Correlation*, edited by W. A. Berggren et al., pp. 51–63, Soc. for Sediment. Geol., Tulsa, Okla.

Channell, J. E. T., C. E. Casellato, G. Muttoni, and E. Erba (2010), Magnetostratigraphy, nannofossil stratigraphy and apparent polar wander for Adria-Africa in the Jurassic-Cretaceous boundary interval, *Palaeogeogr. Palaeoclimatol. Palaeoecol.*, *293*, 51–75, doi:10.1016/j.palaeo.2010.04.030.

Chib, S., and E. Greenberg (1995), Understanding the Metropolis-Hastings algorithm, *Am. Stat.*, *49*, 327–335.

Duijndam, A. J. W. (1988), Bayesian estimation in seismic inversion, part I: Principles, *Geophys. Prospect.*, *36*, 878–898, doi:10.1111/j.1365-2478.1988.tb02198.x.

Fiet, N., and G. Gorin (2000), Lithological expression of Milankovitch cyclicity in carbonate-dominated, pelagic, Barremian deposits in central Italy, *Cretaceous Res.*, *21*, 457–467, doi:10.1006/cres.2000.0220.

Fischer, A. G., and W. Schwarzacher (1984), Cretaceous bedding rhythms under orbital control?, in *Milankovitch and Climate: Understanding the Response to Astronomical Forcing*, edited by A. Berger et al., pp. 163–175, D. Reidel, Dordrecht, Netherlands.

Fischer, A. G., P. L. de Boer, and I. Premoli Silva (1990), Cyclostratigraphy, in *retaceous Resources, Events and Rhythms*, edited by R. N. Ginsburg and B. Beaudoin, pp. 139–172, Kluwer Acad., Dordrecht, Netherlands.

Gee, J. S., and D. V. Kent (2007), Source of oceanic magnetic anomalies and the geomagnetic polarity timescale, in *Treatise on Geophysics*, vol. 5, *Geomagnetism*, edited by G. Schubert, pp. 455–507, Elsevier, Amsterdam, doi:10.1016/B978-044452748-6.00097-3.

Gilks, W. R., S. Richardson, and D. J. Spiegelhalter (Eds.) (1996), *Markov Chain Monte Carlo in Practice*, Chapman and Hall, London.

Gordon, R. G. (1993), Orbital dates and steady rates, *Nature*, *364*, 760–761, doi:10.1038/364760a0.

Gradstein, F. M., J. G. Ogg, and A. G. Smith (Eds.) (2004), *A Geologic Time Scale 2004*, Cambridge Univ. Press, Cambridge, U. K., doi:10.4095/215638.

Handschumacher, D. W., W. W. Sager, T. W. C. Hilde, and D. R. Bracey (1988), Pre-Cretaceous tectonic evolution of the Pacific plate and extension of the geomagnetic polarity reversal timescale with implications for the origin of the Jurassic "quiet zone", *Tectonophysics*, *155*, 365–380, doi:10.1016/0040-1951(88)90275-2.

Hays, J. D., J. Imbrie, and N. J. Shackleton (1976), Variations in the Earth's orbit: Pacemaker of the Ice Ages, *Science*, *194*, 1121–1132, doi:10.1126/science.194.4270.1121.

He, H., Y. Pan, L. Tauxe, H. Qin, and R. Zhu (2008), Toward age determination of the M0r (Barremian-Aptian boundary) of the Early Cretaceous, *Phys. Earth Planet. Inter.*, *169*, 41–48, doi:10.1016/j.pepi.2008.07.014.

Heirtzler, J. R., G. O. Dickson, E. M. Herron, W. C. Pitman III, and X. LePichon (1968), Marine magnetic anomalies, geomagnetic field reversals, and motions of the ocean floor and continents, *J. Geophys. Res.*, *73*, 2119–2136, doi:10.1029/JB073i006p02119.

Herbert, T. D. (1992), Paleomagnetic calibration of Milankovitch cyclicity in Lower Cretaceous sediments, *Earth Planet. Sci. Lett.*, *112*, 15–28, doi:10.1016/0012-821X(92)90003-E.

Herbert, T. D., and A. G. Fischer (1986), Milankovitch climatic origin of mid-Cretaceous black shale rhythms in central Italy, *Nature*, *321*, 739–743, doi:10.1038/321739a0.

Herbert, T. D., I. Premoli Silva, E. Erba, and A. G. Fischer (1995), Orbital chronology of Cretaceous-Paleocene marine sediments, in *Geochronology,*

Timescales, and Stratigraphic Correlation, edited by W. A. Berggren et al., pp. 81–93, Soc. for Sediment. Geol., Tulsa, Okla.

Hilgen, F. J. (1991), Extension of the astronomically calibrated (polarity) time scale to the Miocene/Pliocene boundary, *Earth Planet. Sci. Lett.*, *107*, 349–368, doi:10.1016/0012-821X(91)90082-S.

Hinnov, L. A. (2004), Earth's orbital parameters and cycle stratigraphy, in *A Geologic Time Scale 2004*, edited by F. M. Gradstein, J. G. Ogg, and A. G. Smith, pp. 55–62, Cambridge Univ. Press, Cambridge, U. K.

Hinnov, L. A., and J. G. Ogg (2007), Cyclostratigraphy and the astronomical time scale, *Stratigraphy*, *4*, 239–251.

Hinnov, L. A., and J. Park (1998), Detection of astronomical cycles in the stratigraphic record by frequency modulation (FM) analysis, *J. Sediment. Res.*, *68*, 524–539.

Huang, C., L. A. Hinnov, A. G. Fischer, A. Grippo, and T. D. Herbert (2010), Astronomical tuning of the Aptian Stage from Italian reference sections, *Geology*, *38*, 899–902, doi:10.1130/G31177.1.

Huestis, S. P., and G. D. Acton (1997), On the construction of geomagnetic timescales from non-prejudicial treatment of magnetic anomaly data from multiple ridges, *Geophys. J. Int.*, *129*, 176–182, doi:10.1111/j.1365-246X.1997.tb00947.x.

Jackson, D. D., and M. Matsu'ura (1985), A Bayesian approach to nonlinear inversion, *J. Geophys. Res.*, *90*, 581–591, doi:10.1029/JB090iB01p00581.

Klitgord, K. D., and H. Schouten (1986), Plate kinematics of the central Atlantic, in *The Geology of North America*, vol. M, *The Western North Atlantic Region*, edited by P. R. Vogt and B. E. Tucholke, pp. 351–378, Geol. Soc. of Am., Boulder, Colo.

Krijgsman, W., F. J. Hilgen, I. Raffi, F. J. Sierro, and D. S. Wilson (1999), Chronology, causes and progression of the Messinian salinity crisis, *Nature*, *400*, 652–655, doi:10.1038/23231.

Langereis, C. G., A. A. M. van Hoof, and F. J. Hilgen (1994), Steadying the rates, *Nature*, *369*, 615, doi:10.1038/369615a0.

Larson, R. L., and T. W. C. Hilde (1975), A revised time scale of magnetic reversals for the Early Cretaceous and Late Jurassic, *J. Geophys. Res.*, *80*, 2586–2594, doi:10.1029/JB080i017p02586.

Larson, R. L., and W. C. Pitman III (1972), World-wide correlation of Mesozoic magnetic anomalies, and its implications, *Geol. Soc. Am. Bull.*, *83*, 3645–3662, doi:10.1130/0016-7606(1972)83[3645:WCOMMA]2.0.CO;2.

Laskar, J. (1999), The limits of Earth orbital calculations for geological time-scale use, *Philos. Trans. R. Soc. A*, *357*, 1735–1759, doi:10.1098/rsta.1999.0399.

Laskar, J., P. Robutel, F. Joutel, M. Gastineau, A. C. M. Correia, and B. Levrard (2004), A long-term numerical solution for the insolation quantities of the Earth, *Astron. Astrophys.*, *428*, 261–285, doi:10.1051/0004-6361:20041335.

Laskar, J., A. Fienga, M. Gastineau, and H. Manche (2011), La2010: A new orbital solution for the long-term motion of the Earth, *Astron. Astrophys.*, *532*, A89, doi:10.1051/0004-6361/201116836.

Lourens, L. J., F. J. Hilgen, N. J. Shackleton, J. Laskar, and D. S. Wilson (2004), The Neogene period, in *A Geologic Time Scale 2004*, edited by F. M. Gradstein, J. G. Ogg, and A. G. Smith, pp. 409–440, Cambridge Univ. Press, Cambridge, U. K.

Ludden, J. N. (1992), Radiometric age determination for basement from Sites 765 and 766, Argo Abyssal Plain and northwestern Australian margin, *Proc. Ocean Drill. Program, Sci. Results*, *123*, 3–26.

Mahoney, J. J., R. A. Duncan, M. L. G. Tejada, W. W. Sager, and T. J. Bralower (2005), Jurassic-Cretaceous boundary age and mid-ocean-ridge-type mantle source for Shatsky Rise, *Geology*, *33*, 185–188, doi:10.1130/G21378.1.

Malinverno, A. (2002), Parsimonious Bayesian Markov chain Monte Carlo inversion in a nonlinear geophysical problem, *Geophys. J. Int.*, *151*, 675–688, doi:10.1046/j.1365-246X.2002.01847.x.

Malinverno, A., E. Erba, and T. D. Herbert (2010), Orbital tuning as an inverse problem: Chronology of the early Aptian oceanic anoxic event 1a (Selli Level) in the Cismon APTICORE, *Paleoceanography*, *25*, PA2203, doi:10.1029/2009PA001769.

Martinson, D. G., N. G. Pisias, J. D. Hays, J. Imbrie, T. C. Moore Jr., and N. J. Shackleton (1987), Age dating and the orbital theory of the Ice Ages: Development of a high-resolution 0 to 300,000-year chronostratigraphy, *Quat. Res.*, *27*, 1–29, doi:10.1016/0033-5894(87)90046-9.

Metropolis, N., A. W. Rosenbluth, M. N. Rosenbluth, A. H. Teller, and E. Teller (1953), Equation of state calculations by fast computing machines, *J. Chem. Phys.*, *21*, 1087–1092, doi:10.1063/1.1699114.

Meyers, S. R. (2008), Resolving Milankovitchian controversies: The Triassic Latemar Limestone and the Eocene Green River Formation, *Geology*, *36*, 319–322, doi:10.1130/G24423A.1.

Meyers, S. R., and B. B. Sageman (2007), Quantification of deep-time orbital forcing by average spectral misfit, *Am. J. Sci.*, *307*, 773–792, doi:10.2475/05.2007.01.

Mosegaard, K., and A. Tarantola (1995), Monte Carlo sampling of solutions to inverse problems, *J. Geophys. Res.*, *100*, 12,431–12,447, doi:10.1029/94JB03097.

Müller, R. D., M. Sdrolias, C. Gaina, and W. R. Roest (2008), Age, spreading rates, and spreading asymmetry of the world's ocean crust, *Geochem. Geophys. Geosyst.*, *9*, Q04006, doi:10.1029/2007GC001743.

Ogg, J. G., and A. G. Smith (2004), The geomagnetic polarity time scale, in *A Geologic Time Scale 2004*, edited by F. M. Gradstein, J. G. Ogg, and A. G. Smith, pp. 63–86, Cambridge Univ. Press, Cambridge, U. K.

Ogg, J. G., F. P. Agterberg, and F. M. Gradstein (2004), The Cretaceous period, in *A Geologic Time Scale 2004*, edited by F. M. Gradstein, J. G. Ogg, and A. G. Smith, pp. 409–440, Cambridge Univ. Press, Cambridge, U. K.

Opdyke, N. D., and J. E. T. Channell (1996), *Magnetic Stratigraphy*, Academic, San Diego, Calif.

Pälike, H., R. D. Norris, J. O. Herrle, P. A. Wilson, H. K. Coxall, C. H. Lear, N. J. Shackleton, A. K. Tripati, and B. S. Wade (2006), The heartbeat of the Oligocene climate system, *Science*, *314*, 1894–1898, doi:10.1126/science.1133822.

Park, J., and T. D. Herbert (1987), Hunting for paleoclimatic periodicities in a geologic time series with an uncertain time scale, *J. Geophys. Res.*, *92*(B13), 14,027–14,040, doi:10.1029/JB092iB13p14027.

Pringle, M. S., and R. A. Duncan (1995), Radiometric ages of basement lavas recovered at Loen, Wodejebato, MIT, and Takuto-Daisan guyots, northwestern Pacific Ocean, *Proc. Ocean Drill. Program, Sci. Results*, *144*, 3–26.

Renne, P. R., C. C. Swisher, A. L. Deino, D. B. Karner, T. L. Owens, and D. J. DePaolo (1998), Intercalibration of standards, absolute ages and uncertainties in $^{40}Ar/^{39}Ar$ dating, *Chem. Geol.*, *145*, 117–152, doi:10.1016/S0009-2541(97)00159-9.

Sager, W. W., L. G. Fullerton, R. T. Buffler, and D. W. Handschumacher (1992), Argo Abyssal Plain magnetic lneations revisited: Implications for the onset of seafloor spreading and tectonic evolution of the eastern Indian Ocean, *Proc. Ocean Drill Program, Sci. Results*, *123*, 659–669.

Sager, W. W., M. A. Weiss, M. A. Tivey, and H. P. Johnson (1998), Geomagnetic polarity reversal model of deep-tow profiles from the Pacific Jurassic "Quiet Zone", *J. Geophys. Res.*, *103*, 5269–5286, doi:10.1029/97JB03404.

Sambridge, M., and K. Mosegaard (2002), Monte Carlo methods in geophysical inverse problems, *Rev. Geophys.*, *40*(3), 1009, doi:10.1029/2000RG000089.

Sambridge, M., K. Gallagher, A. Jackson, and P. Rickwood (2006), Trans-dimensional inverse problems, model comparison and the evidence, *Geophys. J. Int.*, *167*, 528–542, doi:10.1111/j.1365-246X.2006.03155.x.

Schwarzacher, W. (1993), *Cyclostratigraphy and the Milankovitch Theory*, Elsevier, Amsterdam.

Sen, M. K., and P. L. Stoffa (1995), *Global Optimization Methods in Geophysical Inversion*, Elsevier, Amsterdam.

Shackleton, N. J., A. Berger, and W. A. Peltier (1990), An alternative astronomical calibration of the lower Pleistocene time scale based on ODP Site 677, *Trans. R. Soc. Edinburgh Earth Sci.*, *81*, 251–261, doi:10.1017/S0263593300020782.

Tarantola, A., and B. Valette (1982), Inverse problems = quest for information, *J. Geophys.*, *50*, 159–170.

Tominaga, M., and W. W. Sager (2010), Revised Pacific M-anomaly geomagnetic polarity time scale, *Geophys. J. Int.*, *182*, 203–232, doi:10.1111/j.1365-246X.2010.04619.x.

Tominaga, M., W. W. Sager, M. A. Tivey, and S.-M. Lee (2008), Deep-tow magnetic anomaly study of the Pacific Jurassic Quiet Zone and implications for the geomagnetic polarity reversal time scale and geomagnetic field behavior, *J. Geophys. Res.*, *113*, B07110, doi:10.1029/2007JB005527.

Wan, X., R. Scott, W. Chen, L. Gao, and Y. Zhang (2011), Early Cretaceous stratigraphy and SHRIMP U-Pb age constrain the Valanginian-Hauterivian boundary in southern Tibet, *Lethaia*, *44*, 231–244, doi:10.1111/j.1502-3931.2010.00238.x.

Wessel, P., and W. H. F. Smith (1991), Free software helps map and display data, *Eos Trans. AGU*, *72*, 441, doi:10.1029/90EO00319.

Wilson, D. S. (1993), Confirmation of the astronomical calibration of the magnetic polarity timescale from sea-floor spreading rates, *Nature*, *364*, 788–790, doi:10.1038/364788a0.